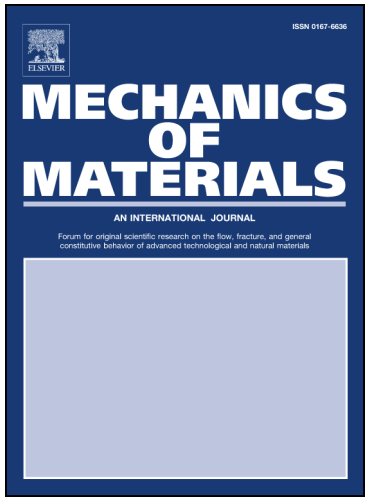

Hardening effects on strain localization predictions in porous ductile materials using the bifurcation approach

Hocine Chalal, Farid Abed-Meraim

PII: S0167-6636(15)00160-X
DOI: http://dx.doi.org/10.1016/j.mechmat.2015.07.012
Reference: MECMAT 2457

To appear in: *Mechanics of Materials*

Received Date: 13 February 2015
Revised Date: 10 July 2015

Please cite this article as: Chalal, H., Abed-Meraim, F., Hardening effects on strain localization predictions in porous ductile materials using the bifurcation approach, *Mechanics of Materials* (2015), doi: http://dx.doi.org/10.1016/j.mechmat.2015.07.012

Hardening effects on strain localization predictions in porous ductile materials using the bifurcation approach

Hocine CHALAL, Farid ABED-MERAIM *

LEM3, UMR CNRS 7239 – Arts et Métiers ParisTech, 4 rue Augustin Fresnel, 57078 Metz Cedex 3, France

DAMAS, Laboratory of Excellence on Design of Alloy Metals for low-mAss Structures, Université de Lorraine, France

Abstract

The localization of deformation into planar bands is often considered as the ultimate stage of strain prior to ductile fracture. In this study, ductility limits of metallic materials are predicted using the Gurson–Tvergaard–Needleman (GTN) damage model combined with the bifurcation approach. Both the GTN constitutive equations and the Rice bifurcation criterion are implemented into the finite element (FE) code ABAQUS/Standard within the framework of large plastic strains and a fully three-dimensional formulation. The current contribution focuses on the effect of strain hardening on ductility limit predictions. It is shown that the choice of void nucleation mechanism has an important influence on the sensitivity of the predicted ductility limits to strain hardening. When strain-controlled nucleation is considered, varying the hardening parameters of the fully dense matrix material has no effect on the porosity evolution and, consequently, very small impact on the predicted ductility limits. For stress-controlled nucleation, the porosity evolution is directly affected by the strain hardening characteristics, which induce a significant effect on the predicted ductility limits. This paper also discusses the use of a micromechanics-based calibration for the GTN q-parameters in the case of strain-controlled nucleation, which is also shown to allow accounting for the hardening effects on plastic strain localization.

Keywords: GTN model, ductile damage, bifurcation criterion, ductility limits, hardening effects

* Corresponding author. Tel.: +(33) 3.87.37.54.79; fax: +(33) 3.87.37.54.70.

E-mail address: farid.abed-meraim@ensam.eu (F. Abed-Meraim).

1 Introduction

In sheet metal forming processes, strain localization occurrence is one of the main defects that limit the formability of stretched sheet metals. A practical approach to characterize the formability of sheet metals is the use of the so-called forming limit diagram (FLD), which consists of a plot of the in-plane critical strains at the onset of localized necking (see, e.g., Keeler and Backofen, 1963; Goodwin,1968). Many literature works have been devoted to the development of theoretical strain localization criteria for the FLD prediction. Two types of necking are usually encountered in stretched metal sheets: diffuse necking and localized necking. In his pioneering work, Considère (1885) proposed a diffuse necking criterion based on the maximum force principle in the particular case of uniaxial tension, while Swift (1952) extended Considère's criterion to the case of in-plane biaxial loading. Alternatively to these two earlier diffuse necking criteria, Hill (1952) developed a different approach for localized necking prediction based on bifurcation theory. This latter criterion indicates that the localized band emerges along a direction of zero extension. However, no bifurcation is predicted with this criterion in the expansion domain of the FLD. To overcome this limitation, Hill's localized necking criterion may be combined with Swift's diffuse necking criterion to determine a complete FLD of a sheet metal. Another approach for localized necking prediction, which is referred to as the M–K criterion, assumes the existence of an initial geometric imperfection (Marciniak and Kuczynski, 1967) or an initial material imperfection (see, e.g., Yamamoto, 1978) in the sheet metal. This M–K approach is one of the most commonly used criteria for the determination of FLDs, due to its simple use and its applicability to a wide range of constitutive models. Note also that Hora et al. (1996) proposed a modification to Considère's maximum force criterion to take the strain-path dependency into account in the prediction of localized necking. Other theoretical criteria based on bifurcation theory have been developed in the literature during the last few decades

(see, e.g., Abed-Meraim et al. (2014) for a detailed discussion and comparison). In this regard, Hill (1958) developed a general bifurcation (GB) criterion based on the loss of uniqueness for the solution of the associated boundary value problem. This GB criterion, written in a local framework, allows predicting the onset of diffuse necking in sheet metals. A condition less conservative than the BG criterion has been proposed by Valanis (1989), and corresponds to the stationarity of the stress state. Analogous approaches based on bifurcation theory have been established in Rudnicki and Rice (1975), Stören and Rice (1975) and Rice (1976) to predict localized necking or shear band instabilities in solid materials. In these criteria, the occurrence of localization bifurcation is related to the loss of ellipticity of the associated boundary value problem.

The above criteria are generally coupled with constitutive models for the prediction of critical strains. In Rudnicki and Rice (1975) and Rice (1976), it has been shown that, in the framework of phenomenological constitutive models with associated plasticity and smooth yield surface, localization bifurcation cannot be predicted in the positive hardening regime. In such a situation, damage-induced softening is required in the constitutive model. In the literature, damage models may be classified into two main theories. The first is the continuum damage mechanics approach (see, e.g., Lemaitre, 1985; Kachanov, 1986; Lemaitre, 1992), where damage is described by a phenomenological variable, which may be isotropic scalar or anisotropic tensor-valued, representing a surface density of defects. The second theory is based on micromechanical analysis of void growth, which describes the complex ductile damage mechanisms in porous materials. In this regard, Gurson (1977) proposed a void growth model that takes into consideration the effect of hydrostatic stress on porous materials. Later, several modifications of the Gurson model have been made to account for void nucleation, coalescence, hardening of the dense matrix, and plastic anisotropy (see, e.g., Chu and Needleman, 1980; Tvergaard, 1981, 1982a, 1982b, Tvergaard and Needleman, 1984; Benzerga and Besson, 2001). In the so-called Gurson–Tvergaard–Needleman (GTN) model,

the void volume fraction acts as a damage internal variable responsible for the progressive loss of load carrying capacity. In the present work, the GTN model with isotropic hardening, for the fully dense matrix material, and a von Mises yield criterion is considered to describe ductile damage in porous materials.

More specifically, in the current contribution, an approach that combines the GTN model with the Rice bifurcation criterion is proposed to predict ductility limits of porous materials. To this end, the resulting coupling is implemented into the finite element (FE) code ABAQUS/Standard in the framework of large plastic strains and a fully three-dimensional formulation. In a recent work, a similar approach has been followed (see Mansouri et al., 2014) to investigate the effects of hardening and damage parameters on the prediction of ductility limits of porous materials. In this latter study, it has been shown that the damage parameters have a significant effect on the ductility limits for all of the strain paths considered, while the effect of strain hardening was only perceptible for the plane strain tension loading path. These results, which have been found in the case of strain-controlled nucleation, are explained by the fact that, in such nucleation modeling, the porosity evolution is totally governed by the damage parameters. To reproduce the effect of strain hardening of the dense matrix on the ductility limits, as classically observed in the literature (see, e.g., Yamamoto, 1978; Hora et al., 1996; Zhao et al., 1996), a micromechanics-based calibration for the GTN q-parameters is adopted in the current study, as suggested by Faleskog et al. (1998), in order to account for the strain hardening effect on the porosity evolution. Alternatively, for the same purpose, stress-controlled nucleation is also considered in this study within the GTN model (see, e.g., Needleman and Rice, 1978; Chu and Needleman, 1980; Saje et al., 1982), which allows the strain hardening effect on the porosity evolution to be accounted for. In this latter case, the normality of the plastic flow rule does not hold, which induces a destabilizing effect that promotes strain localization.

2 Porous elastic–plastic constitutive equations

The so-called GTN damage model, which is an extension of the original Gurson model (1977), is briefly described in this section. Only the main constitutive equations are recalled; the full details can be found in Tvergaard (1982c) and Tvergaard and Needleman (1984).

2.1 Large strain kinematics

Within the large strain framework, the material behavior is commonly described by rate constitutive equations and, to achieve material objectivity, objective rates must be used. To this end, the constitutive models are often written in a convenient frame in order to simplify their formulation and further their FE implementation. The large deformation theory used here, which is also consistent with that adopted in the FE code ABAQUS, is recalled hereafter.

The kinematics of large elastic–plastic deformation are based on the multiplicative decomposition of the deformation gradient $\mathbf{F}$ into a plastic part $\mathbf{F}^p$ and an elastic part $\mathbf{F}^e$

$$\mathbf{F} = \mathbf{F}^e \cdot \mathbf{F}^p, \qquad \mathbf{F}^e \cong \left(\mathbf{1} + \boldsymbol{\varepsilon}^e\right) \cdot \mathbf{R}. \tag{1}$$

In Eq. (1), the elastic strains are considered to be small with respect to unity, which is a reasonable assumption for sheet metals; nevertheless, large rotations are rigorously considered. Here, $\mathbf{1}$ is the second-order identity tensor, $\boldsymbol{\varepsilon}^e$ is the symmetric tensor of small elastic strains ($\left|\boldsymbol{\varepsilon}^e\right| << 1$), and $\mathbf{R}$ is the rotation tensor. The velocity gradient $\mathbf{L}$, the strain rate tensor $\mathbf{D}$ and the material spin $\mathbf{W}$ are given by

$$\mathbf{L} = \dot{\mathbf{F}} \cdot \mathbf{F}^{-1} = \dot{\mathbf{R}} \cdot \mathbf{R}^T + \mathbf{D}^e + \mathbf{R} \cdot \dot{\mathbf{F}}^p \cdot \left(\mathbf{F}^p\right)^{-1} \cdot \mathbf{R}^T, \tag{2}$$

$$\mathbf{D} = \tfrac{1}{2}(\mathbf{L} + \mathbf{L}^T) = \mathbf{D}^e + \mathbf{D}^p, \qquad \mathbf{W} = \tfrac{1}{2}(\mathbf{L} - \mathbf{L}^T), \tag{3}$$

where $\mathbf{D}^e$ and $\mathbf{D}^p$ are the objective time derivative of the elastic strain tensor and the plastic strain rate, respectively, given by the following expressions:

$$\mathbf{D}^e = \dot{\boldsymbol{\varepsilon}}^e + \boldsymbol{\varepsilon}^e \cdot \dot{\mathbf{R}} \cdot \mathbf{R}^T - \dot{\mathbf{R}} \cdot \mathbf{R}^T \cdot \boldsymbol{\varepsilon}^e = \overset{\circ}{\boldsymbol{\varepsilon}}{}^e, \qquad \mathbf{D}^p = \mathbf{R} \cdot \left[\dot{\mathbf{F}}^p \cdot \left(\mathbf{F}^p\right)^{-1}\right]^{sym} \cdot \mathbf{R}^T, \tag{4}$$

where $[\ ]^{sym}$ designates the symmetric part.

Formulating the constitutive equations within the large strain framework requires the use of such objective rates. A very convenient approach consists in reformulating these equations in terms of rotation-compensated variables. More precisely, if $\mathbf{A}$ and $\mathbf{B}$ denote second and fourth-order tensors, respectively, the associated rotation-compensated tensors are defined as

$$\hat{A}_{ij} = \mathfrak{R}_{ki}\mathfrak{R}_{lj}A_{kl}, \qquad \hat{B}_{ijkl} = \mathfrak{R}_{pi}\mathfrak{R}_{qj}\mathfrak{R}_{rk}\mathfrak{R}_{sl}B_{pqrs}, \tag{5}$$

where $\mathfrak{R}$ is an orthogonal rotation matrix that is generated by a skew-symmetric spin tensor $\mathbf{\Omega}$ using the rate equation $\dot{\mathfrak{R}}\cdot\mathfrak{R}^T = \mathbf{\Omega}$.

The main advantage of this approach is that objective derivatives defined like in Eq. (4) by $\overset{\circ}{\mathbf{A}} = \dot{\mathbf{A}} + \mathbf{A}\cdot\mathbf{\Omega} - \mathbf{\Omega}\cdot\mathbf{A}$, are simply related to the material time derivatives of their rotation-compensated counterparts via equations similar to Eq. (5), *i.e.*

$$\dot{\hat{A}}_{ij} = \mathfrak{R}_{ki}\mathfrak{R}_{lj}\overset{\circ}{A}_{kl}, \qquad \dot{\hat{B}}_{ijkl} = \mathfrak{R}_{pi}\mathfrak{R}_{qj}\mathfrak{R}_{rk}\mathfrak{R}_{sl}\overset{\circ}{B}_{pqrs}. \tag{6}$$

For example, the Jaumann derivative is obtained by setting $\mathbf{\Omega} = \mathbf{W}$, while using $\mathfrak{R} = \mathbf{R}$ leads to the Green–Naghdi derivative. Jaumann rates are considered throughout the present work. In what follows, all variables are written in the associated co-rotational frame, that is to say, with the rotation-compensated variables. Consequently, simple time derivatives are involved in the constitutive equations developed in section 2.2, making them identical in form to a small-strain formulation. For simplicity, the superposed hat (^) will be omitted hereafter.

2.2 GTN yield function and evolution equations of internal variables

The isotropic GTN yield condition based on spherical voids has the following form:

$$\mathrm{F} = \left(\frac{\sigma_{eq}}{\sigma_{\mathrm{M}}}\right)^2 + 2q_1 f^* \cosh\left(\frac{3}{2}q_2\frac{\sigma_m}{\sigma_{\mathrm{M}}}\right) - \left(1 + q_3 f^{*2}\right) \le 0, \tag{7}$$

where $\sigma_{eq} = \sqrt{3\mathbf{S}:\mathbf{S}/2}$ is the macroscopic von Mises equivalent stress, $\sigma_m = \frac{1}{3}\boldsymbol{\sigma}:\mathbf{1}$ is the hydrostatic stress, and $\mathbf{S} = \boldsymbol{\sigma} - \sigma_m\mathbf{1}$ denotes the deviatoric part of the macroscopic Cauchy stress tensor $\boldsymbol{\sigma}$. The tensile flow stress $\sigma_{\mathrm{M}}\left(\bar{\varepsilon}_{\mathrm{M}}^{\mathrm{pl}}\right)$ of the fully dense material is a function of

the equivalent plastic strain $\bar{\varepsilon}_{\mathrm{M}}^{\mathrm{pl}}$ of the matrix surrounding the voids. In Eq. (7), q_1, q_2 and q_3 are material parameters, while $f^*(f)$ is the modified void volume fraction, which accounts for the void coalescence mechanism as follows:

$$f^*(f)=\begin{cases} f & \text{for} \quad f \le f_{cr}, \\ f_{cr}+\delta_{GTN}\left(f-f_{cr}\right) & \text{for} \quad f_{cr}<f\le f_R, \end{cases} \quad \text{with} \quad \delta_{GTN}=\frac{f_u^*-f_{cr}}{f_R-f_{cr}}, \tag{8}$$

where f represents the actual void volume fraction. The critical void volume fraction f_{cr} marks the onset of the void coalescence stage. The final fracture of the material, corresponding to the complete loss of material stress carrying capacity, is reached for a void volume fraction f_R, which corresponds to a modified void volume fraction f_u^*.

The matrix material is assumed to obey isotropic hardening defined as follows:

$$\dot{\sigma}_{\mathrm{M}}=h\dot{\bar{\varepsilon}}_{\mathrm{M}}^{\mathrm{pl}}, \tag{9}$$

where $h\left(\bar{\varepsilon}_{\mathrm{M}}^{\mathrm{pl}}\right)$ is the plastic hardening modulus of the fully dense matrix material.

The plastic flow is described by the classical relationship, involving the derivative of the yield function with respect to the stress (i.e., normal to the yield surface in the stress space)

$$\mathbf{D}^{\mathrm{p}}=\dot{\lambda}\frac{\partial \mathrm{F}}{\partial \boldsymbol{\sigma}}, \tag{10}$$

where $\dot{\lambda}$ is the plastic multiplier to be determined by the consistency condition $\dot{\mathrm{F}}=0$.

The incremental change in void volume fraction originates from two contributions: the growth of existing voids and nucleation of new ones (Chu and Needleman, 1980), which writes

$$\dot{f}=\dot{f}_{\mathrm{growth}}+\dot{f}_{\mathrm{nucleation}}, \tag{11}$$

where

$$\dot{f}_{\mathrm{growth}}=\left(1-f\right)\mathbf{D}^{p}:\mathbf{1} \qquad ; \qquad \dot{f}_{\mathrm{nucleation}}=\left[\frac{A_N}{h}+B_N\right]\dot{\sigma}_{\mathrm{M}}+B_N\dot{\sigma}_m. \tag{12}$$

Taking $A_N>0$ and $B_N=0$, the void nucleation is strain-controlled, while it is stress-controlled for $A_N=0$ and $B_N>0$, with A_N and B_N defined by normal distribution laws

$$A_N = \frac{f_N}{s_N\sqrt{2\pi}}\exp\left[-\frac{1}{2}\left(\frac{\bar{\varepsilon}_{\mathrm{M}}^{\mathrm{pl}} - \varepsilon_N}{s_N}\right)^2\right], \qquad B_N = \frac{f_N}{s_N\sigma_0\sqrt{2\pi}}\exp\left(-\frac{1}{2}\left(\frac{\sigma_{\mathrm{M}} + \sigma_m - \sigma_N}{s_N\sigma_0}\right)^2\right), \quad (13)$$

where f_N is the volume fraction of the inclusions that are likely to nucleate, ε_N and σ_N are, respectively, the mean strain and the mean stress for nucleation, s_N is the standard deviation on ε_N and σ_0 is the initial yield stress of the dense matrix.

In the co-rotational frame defined in section 2.1, which corresponds to adopting a Jaumann-type objective rate, the stress–strain relationship is given by the hypoelastic law

$$\dot{\boldsymbol{\sigma}} = \mathbf{C}^e : \left(\mathbf{D} - \dot{\lambda}\frac{\partial \mathrm{F}}{\partial \boldsymbol{\sigma}}\right) = \mathbf{C}^{ep} : \mathbf{D}, \quad (14)$$

where $\mathbf{C}^e$ is the elasticity tensor, while $\mathbf{C}^{ep}$ is the elastic–plastic tangent modulus obtained as

$$\mathbf{C}^{ep} = \mathbf{C}^e - \frac{\mathbf{P}\otimes\mathbf{Q}}{H_\lambda}, \quad (15)$$

where

$$\mathbf{P} = \mathbf{C}^e : \frac{\partial \mathrm{F}}{\partial \boldsymbol{\sigma}} \quad ; \quad \mathbf{Q} = \mathbf{M} : \mathbf{C}^e \quad \text{with} \quad \mathbf{M} = \frac{\partial \mathrm{F}}{\partial \boldsymbol{\sigma}} + \frac{B_N}{3}\frac{\partial \mathrm{F}}{\partial f^*}\frac{\partial f^*}{\partial f}\mathbf{1}, \quad (16)$$

and

$$H_\lambda = \mathbf{M} : \mathbf{C}^e : \frac{\partial \mathrm{F}}{\partial \boldsymbol{\sigma}} - \frac{h}{(1-f)}\frac{\boldsymbol{\sigma} : \dfrac{\partial \mathrm{F}}{\partial \boldsymbol{\sigma}}}{\sigma_{\mathrm{M}}}\left[\frac{\partial \mathrm{F}}{\partial \sigma_{\mathrm{M}}} + \left(\frac{A_N}{h} + B_N\right)\frac{\partial \mathrm{F}}{\partial f^*}\frac{\partial f^*}{\partial f}\right] - (1-f)\frac{\partial f^*}{\partial f}\frac{\partial \mathrm{F}}{\partial f^*}\frac{\partial \mathrm{F}}{\partial \boldsymbol{\sigma}} : \mathbf{1}. \quad (17)$$

For strain-controlled nucleation (i.e., $A_N > 0$ and $B_N = 0$), $\mathbf{P} = \mathbf{Q}$ and the normality of the plastic flow rule holds. In such a case, the elastic–plastic tangent modulus given by Eq. (15) becomes symmetric. For stress-controlled nucleation (i.e., $A_N = 0$ and $B_N > 0$), the normality of the plastic flow rule does not hold and the tangent modulus in Eq. (15) is non-symmetric. This apparent non-normality property comes from the dependence of the void nucleation rate on the hydrostatic stress (see Eq. (12)) via the non-zero parameter B_N. Such non-normality in the plastic flow rule, which leads to a non-symmetric elastic–plastic tangent modulus, has important consequences and will play an important role in strain localization analysis.

2.3 Implementation of the constitutive equations and its validation

2.3.1 Time integration scheme

In this section, the explicit scheme used for the time integration of the GTN constitutive equations is briefly described. The resulting algorithm is implemented into the commercial finite element code ABAQUS/Standard via a user-defined material subroutine (UMAT), using a co-rotational frame, which corresponds to adopting a Jaumann-type objective rate. For each integration point of the finite elements, ABAQUS provides to the UMAT the stress state and other internal variables at the beginning of loading increment. Then, the UMAT has to return to ABAQUS the updated stress state and internal variables at the end of the loading increment. For the static implicit solver ABAQUS/Standard, the computation of the consistent tangent modulus is also required in order to solve the global finite element equilibrium equations at the end of loading increment.

Considering the GTN model presented in the previous section, it is easily shown that the evolution of the various internal variables can be written in the form of the following global differential equation:

$$\dot{\mathbf{x}} = \mathbf{h}_{\mathbf{x}}\left(\mathbf{x}\right), \tag{18}$$

where vector $\mathbf{x}$ contains all of the GTN model variables to be updated at the end of increment (see Eqs. (10)–(12) and (14)). This compact rate form can encompass various evolution laws for the material behavior (hardening descriptions, porosity evolutions, advanced yield surfaces), and its time integration can be easily achieved using an explicit scheme.

In this work, a simple explicit time integration scheme is adopted to update the stresses and state variables of the GTN model. In such a scheme, the stresses and the state variables at the end of loading increment are calculated as functions of all variables at the beginning of loading increment. This straightforward integration algorithm is a reasonable compromise in terms of computational efficiency, accuracy and convergence. Indeed, explicit time

integration does not involve matrix inversion or iterative procedures for convergence, unlike implicit time integration. However, for explicit schemes, the time increment must be kept small enough to ensure accuracy and stability (see, e.g., Li and Nemat-Nasser, 1993; Kojic, 2002; Oliver et al., 2005).

More specifically, the forward fourth-order Runge–Kutta method is employed here for the integration of the rate equations using the compact form of Eq. (18) expressed in the material co-rotational frame. The full details for all steps as well as sub-increment calculations can be found in Mansouri et al. (2014) and will not be repeated here for conciseness.

2.3.2 Validation of the numerical implementation

The first validation test is taken from Aravas (1987), who provided an exact solution for the hydrostatic tension of a porous medium described by the original Gurson model, in which nucleation is strain-controlled, while coalescence is not considered. The material parameters for the simulation are as follows: $\sigma_0 / E = 1/300$, where σ_0 is the initial tensile yield stress, $\nu = 0.3$, $f_0 = 0.04$ for the initial porosity, $s_N = 0.1$, $\varepsilon_N = 0.3$, $f_N = 0.04$, $q_1 = 1.5$, $q_2 = 1$, and $q_3 = 2.25$. The isotropic hardening of the fully dense matrix material is governed by the following law:

$$\frac{\sigma_{\mathrm{M}}}{\sigma_0} = \left(\frac{\sigma_{\mathrm{M}}}{\sigma_0} + \frac{3G}{\sigma_0} \bar{\varepsilon}_{\mathrm{M}}^{\mathrm{pl}} \right)^n , \tag{19}$$

where $n = 0.1$ and $G = E/2(1+\nu)$ is the elastic shear modulus. The predictions of the GTN model implemented in the UMAT subroutine are compared in Fig. 1 to both the reference results of Aravas (1987) and the results given by the built-in GTN model available in ABAQUS/Standard. It can be observed from Fig. 1 that the three simulation results coincide, provided that the loading increments are taken sufficiently small.

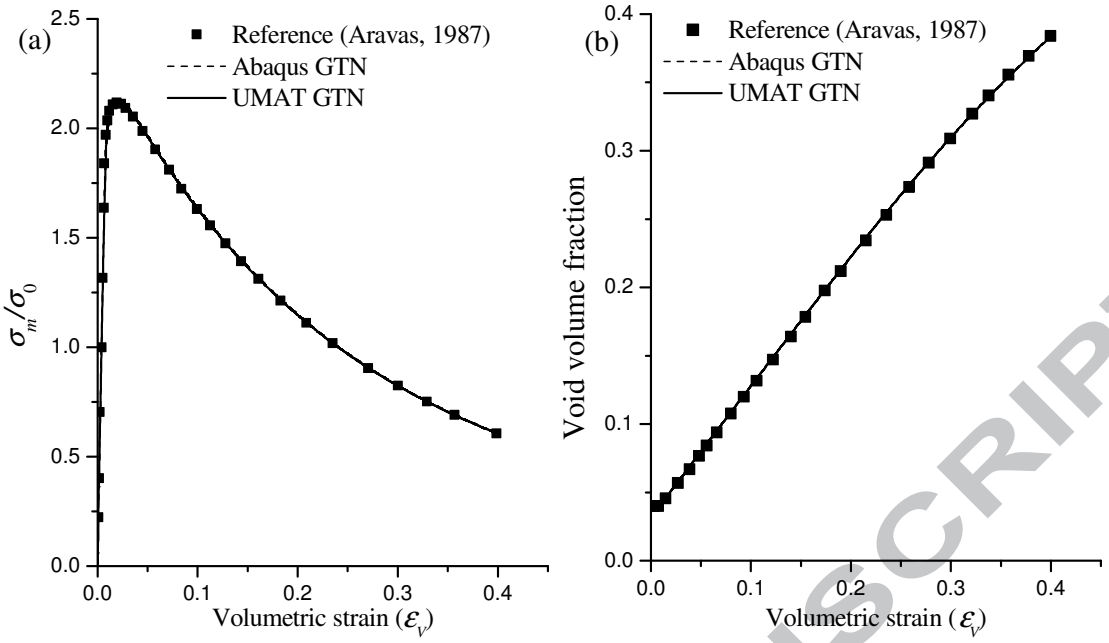

Fig. 1. Confrontation of the predictions from the UMAT subroutine, the built-in GTN model available in ABAQUS/Standard, and the exact solution of Aravas (1987) for a purely hydrostatic loading: normalized hydrostatic stress (a) and porosity (b) as functions of volumetric strain.

The second simulation allows us to estimate the size of strain increments required to obtain a sufficiently accurate solution. Hence, the accuracy of the time integration scheme used to implement the GTN model is investigated here. The results obtained by the implemented GTN model with different strain increment sizes are compared to those yielded by the built-in GTN model available in ABAQUS/Explicit. In the same way as in the previous test, nucleation is taken strain-controlled; however, the current simulation accounts for the coalescence stage. The hardening and damage parameters used for this simulation, which correspond to a typical aluminum alloy, are summarized in Tables 1 and 2, respectively. For this material, the Ludwig isotropic hardening model is considered, which is defined by

$$\sigma_{\mathrm{M}} = \sigma_0 + k\left(\bar{\varepsilon}_{\mathrm{M}}^{\mathrm{pl}}\right)^n . \tag{20}$$

Table 1

Elastic properties and Ludwig hardening parameters.

Material	E (MPa)	ν	σ_0 (MPa)	k (MPa)	n
Aluminum	70,000	0.33	140	200	0.1

Table 2

Damage parameters of the GTN model.

Material	f_0	s_N	ε_N	f_N	f_{cr}	δ_{GTN}	q_1	q_2	q_3
Aluminum	0.001	0.1	0.30	0.04	0.01	20	1.5	1.0	2.25

In Fig. 2, the numerical results for a uniaxial tensile test obtained with the implemented GTN model are compared to the reference results given by the built-in ABAQUS GTN model, the latter being obtained by an implicit time integration scheme. It is shown that the size of strain increments should be taken smaller than 10^{-5} in order to ensure sufficient accuracy for both the stress−strain response (Fig. 2(a)), and the porosity evolution (Fig. 2(b)). These results also demonstrate the ability of the implemented model to reproduce the sudden drop in the stress−strain response after the onset of the coalescence stage.

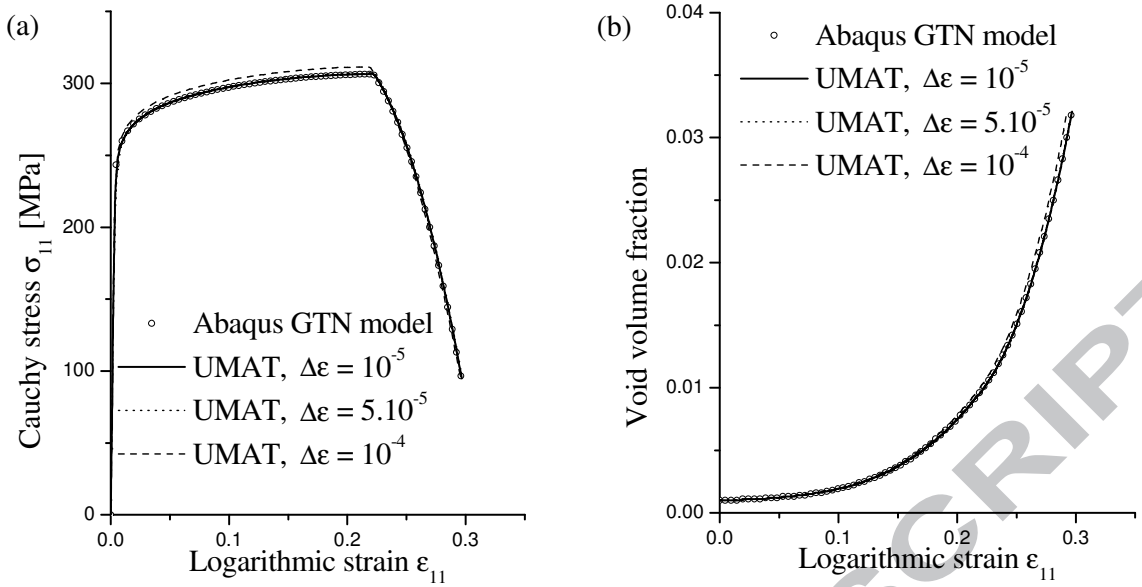

Fig. 2. Numerical simulations for a uniaxial tensile test obtained from the built-in ABAQUS model and the implemented UMAT subroutine: (a) stress−strain curves and (b) evolution of void volume fraction.

3 Strain localization modeling

To predict the ductility limits of materials, the strain localization criterion proposed by Rice and co-workers (see Rudnicki and Rice, 1975; Rice, 1976) is adopted in this study. This material instability criterion is based on bifurcation theory, where the critical condition is viewed as the loss of uniqueness for the solution of the rate equilibrium equations, with a bifurcation mode in the form of an infinite localization band (see Fig. 3).This bifurcation approach assumes that the incipience of the localization band, which is defined by its unit normal **n** (see Fig. 3), is sought within a homogeneous strain field of the solid, where all geometric instabilities are excluded.

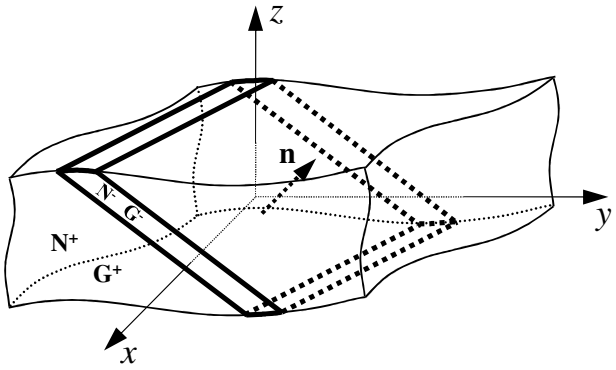

Fig. 3. Schematic illustration of the occurrence of a localization band in an infinite block of material.

In the framework of large strains, the nominal stress rate $\dot{\mathbf{N}}$ is related to the velocity gradient $\mathbf{G}$ by the following relationship:

$$\dot{\mathbf{N}} = \boldsymbol{\mathcal{L}} : \mathbf{G}, \tag{21}$$

where $\boldsymbol{\mathcal{L}}$ is a fourth-order tangent modulus, which needs to be determined in terms of the analytical elastic–plastic tangent modulus (see Eq. (15)), and some tensors involving Cauchy stress components. The localization condition can be derived from the equilibrium and compatibility conditions along the localization band, by expressing the normal continuity of the nominal stress rate vector through the discontinuity surfaces

$$\mathbf{n} \cdot [\![\dot{\mathbf{N}}]\!] = \mathbf{0}, \tag{22}$$

where $[\![\dot{\mathbf{N}}]\!] = \dot{\mathbf{N}}^{+} - \dot{\mathbf{N}}^{-}$ represents the jump in the nominal stress rate across the discontinuity surfaces of the localization band. Furthermore, Maxwell's compatibility condition states that the jump in the velocity gradient can be expressed in the following form:

$$[\![\mathbf{G}]\!] = \dot{\mathbf{c}} \otimes \mathbf{n}, \tag{23}$$

where vector $\dot{\mathbf{c}} = [\![\mathbf{G}]\!] \cdot \mathbf{n}$ defines the localization mode (e.g., shear mode when $\dot{\mathbf{c}} \perp \mathbf{n}$), which must be non-zero for effective bifurcation. Combining Eqs. (21)–(23), the following linear system can be derived:

$$\left(\mathbf{n} \cdot \boldsymbol{\mathcal{L}} \cdot \mathbf{n}\right) \cdot \dot{\mathbf{c}} = \mathbf{0}\,. \tag{24}$$

Finally, the critical condition, which corresponds to the loss of ellipticity of the associated boundary value problem, is given by the following criterion (Rice, 1976):

$$\det \mathbf{H} = \det\left(\mathbf{n} \cdot \boldsymbol{\mathcal{L}} \cdot \mathbf{n}\right) = 0\,, \tag{25}$$

where $\mathbf{H} = \mathbf{n} \cdot \boldsymbol{\mathcal{L}} \cdot \mathbf{n}$ is the so-called acoustic tensor. The expression of the tangent modulus $\boldsymbol{\mathcal{L}}$ involved in Eqs. (21) and (25) is given by

$$\boldsymbol{\mathcal{L}} = \mathbf{C}^{ep} + \mathbf{T}_1 - \mathbf{T}_2 - \mathbf{T}_3\,, \tag{26}$$

where $\mathbf{T}_1$, $\mathbf{T}_2$ and $\mathbf{T}_3$ are fourth-order tensors that originate from the large strain framework. Their expressions only depend on Cauchy stress components, as can be seen through the following expressions (see, e.g., Mansouri et al., 2014; Haddag et al., 2009):

$$\begin{cases} T_{1ijkl} = \sigma_{ij}\delta_{kl} \\ T_{2ijkl} = \dfrac{1}{2}\left(\delta_{ik}\sigma_{jl} + \delta_{il}\sigma_{jk}\right). \\ T_{3ijkl} = \dfrac{1}{2}\left(\sigma_{ik}\delta_{jl} - \sigma_{il}\delta_{jk}\right) \end{cases} \tag{27}$$

It is worth noting that in the case of the small strain framework, only the analytical tangent modulus $\mathbf{C}^{ep}$ is involved in the expression of the tangent modulus $\boldsymbol{\mathcal{L}}$.

4 Ductility limit predictions

In this study, the present GTN model is combined with the above-described Rice bifurcation criterion to predict the ductility limits of steel and aluminum materials. The isotropic hardening law considered in the GTN model for the fully dense matrix material is of power type. The effect of strain hardening on the prediction of strain localization is investigated in this section, by varying the hardening exponent of the power-type law. First, the classical GTN model with strain-controlled nucleation is combined with the Rice criterion. For this GTN model, it has been shown by several authors (see, e.g., Leblond et al., 1995; Faleskog et al., 1998; Gao et al., 1998) that the porosity evolution does not depend on strain hardening. Second, following the work of Faleskog and co-workers (see Faleskog et al., 1998), the GTN model is used in conjunction with micromechanics calibration of porosity growth, via the q parameters, in order to take the strain hardening effect into account. Finally, stress-controlled nucleation is considered in the GTN model, leading to non-normality in the plastic flow rule, which in turn provides a destabilizing effect that promotes earlier strain localization.

4.1 Case of strain-controlled nucleation

Strain-controlled nucleation is considered in this section, by taking the Gaussian amplitudes $A_N > 0$ and $B_N = 0$ in the GTN model (see Eq. (13)). Therefore, normality of the plastic flow rule holds, and the analytical elastic–plastic tangent modulus $\mathbf{C}^{ep}$ (see Eq. (15)) is symmetric. However, the tangent modulus $\mathcal{L}$ involved in the acoustic tensor $\mathbf{H}$ (see Eqs. (25) and (26)) is not symmetric due to the convective stress components (see Eqs. (26) and (27)). The resulting constitutive model is coupled with the bifurcation criterion to analyze the effect of strain hardening on the ductility limits of aluminum alloy and steel materials. The isotropic hardening model used in this study follows the Ludwig power law (see Eq. (20)).

For these materials, the hardening parameters are summarized in Table 3, while the damage parameters are taken from Brunet et al. (1998), as reported in Table 4.

Table 3

Elastic properties and Ludwig hardening parameters.

Material	E (MPa)	ν	σ_0 (MPa)	k (MPa)	n
Aluminum	70,000	0.33	140	370	0.1-0.2-0.3
Steel	198,000	0.3	150	550	0.1-0.2-0.3

Table 4

Damage parameters for the GTN model with strain-controlled nucleation.

Material	f_0	s_N	ε_N	f_N	f_{cr}	δ_{GTN}	q_1	q_2	q_3
Aluminum	0.001	0.1	0.27	0.035	0.00213	10	1.5	1.0	2.15
Steel	0.001	0.1	0.50	0.040	0.040	5	1.5	1.0	2.15

Figures 4(a) and 4(b) illustrate the effect of the hardening exponent n on the predicted ellipticity loss diagrams (ELDs) for the steel and aluminum alloy, respectively. For both materials, it can be seen that varying the hardening exponent n has a small effect on strain localization predictions except for loading paths near the plane strain tension, where a slightly more noticeable effect is observed. These trends have already been found in Mansouri et al. (2014) for similar materials using the same GTN model, with strain-controlled nucleation, coupled with the Rice bifurcation criterion. In that earlier contribution, the Swift hardening law was used and a sensitivity analysis was carried out for the whole set of hardening parameters (i.e., yield stress σ_0, k parameter, and hardening exponent n). Various reasons were discussed in Mansouri et al. (2014) to explain this apparent insensitivity of strain localization to hardening parameters. It has been shown through parametric studies that

damage is the dominant mechanism in the approach combining the GTN model, with strain-controlled nucleation, and the Rice bifurcation criterion. In particular, damage has been shown to have a significant influence on strain localization, which occurs at strongly negative hardening modulus for most of the loading paths. An example of this is illustrated in Fig. 5, where the evolution of the Cauchy stress and void volume fraction, up to localization, is given for the aluminum alloy under balanced biaxial tension (BBT) loading path. The stress–strain curves in Fig. 5(a) reveal that strain localization requires a strongly negative hardening modulus for this loading path. Moreover, Fig. 5(b) shows that the porosity evolution, based on strain-controlled nucleation, does not depend on the strain hardening of the fully dense matrix. This limitation is attributed to the original Gurson model, which was developed on the assumption of an ideal-plastic matrix material surrounding the voids, as has already been pointed out in Leblond et al. (1995).

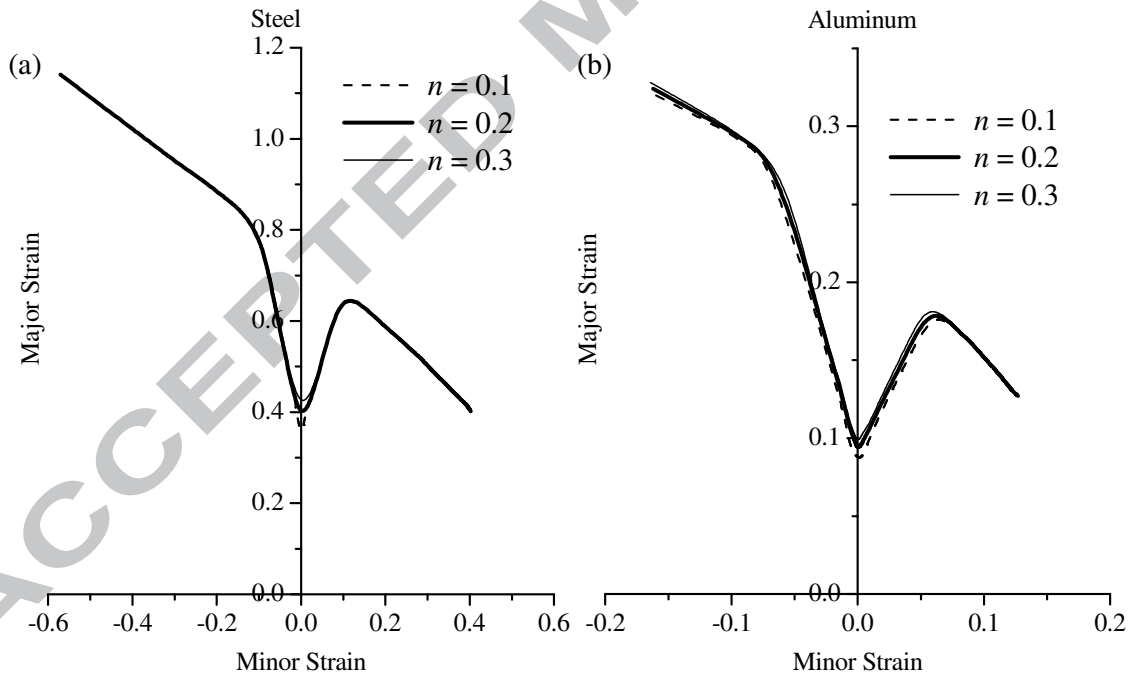

Fig. 4. Effect of the hardening exponent n of the Ludwig hardening law on the prediction of the ELDs for aluminum alloy and steel materials.

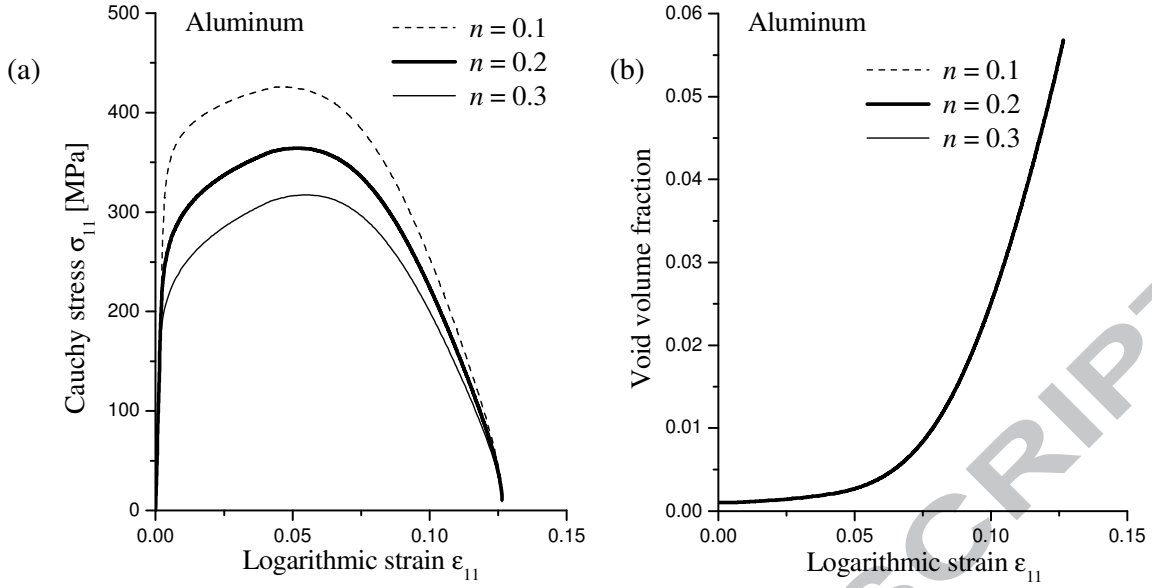

Fig. 5. Stress–strain response and void volume fraction evolution, up to localization, for the aluminum alloy under BBT strain path.

Note that for the plane strain tension (PST) loading path, the effect of the hardening exponent n on the ductility limits is more pronounced than for the other loading paths (see Fig. 4). Indeed, according to earlier investigations (see, e.g., Yamamoto, 1978), localization is expected to occur at a critical hardening modulus close to zero under plane strain tension. This observation is confirmed by the results reported in Fig. 6(a), where the localization points are predicted around the peak of the Cauchy stress–strain curves for the aluminum alloy under PST strain path. Moreover, Fig. 6(b) shows that the porosity levels are much lower for the PST loading path. This suggests that, unlike the other strain paths, damage is not the only dominant destabilizing mechanism along the PST strain path, for which strain hardening still has some non-negligible contribution. Similar results are obtained for steel materials and are not reported here for conciseness. In order to emphasize more this hardening effect, Fig. 7 shows the evolution of the critical localization strain as a function of initial porosity for different values of the hardening exponent n. This figure clearly highlights the dependence of critical strain on the strain hardening exponent n for the PST loading path. The results of this study, given by the GTN model, are consistent with those reported in

Yamamoto (1978), where the original Gurson model restricted to the only void growth mechanism has been used.

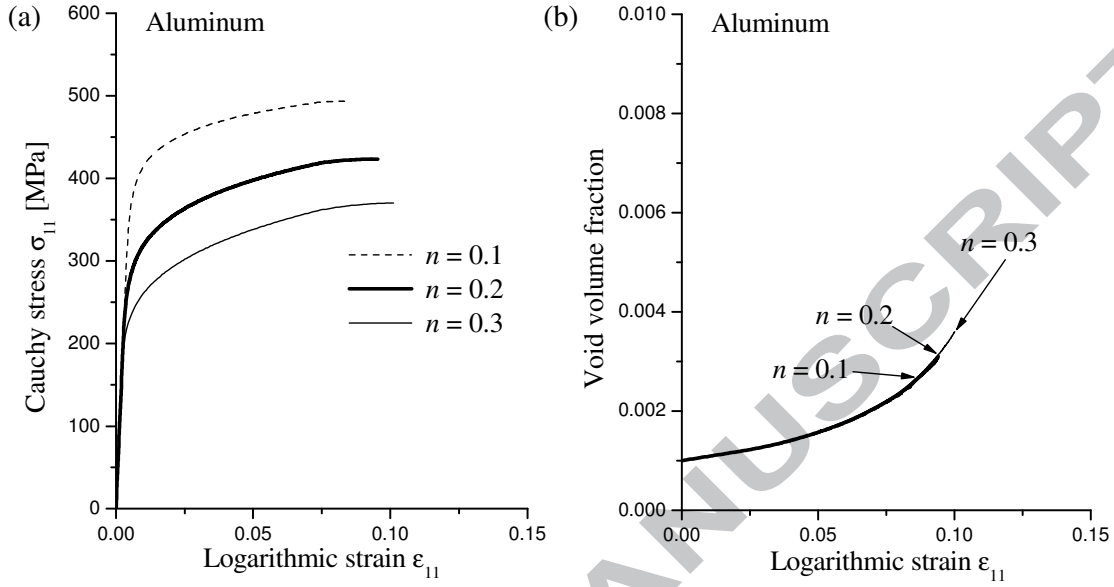

Fig. 6. Stress–strain response and void volume fraction evolution, up to localization, for the aluminum alloy under PST strain path.

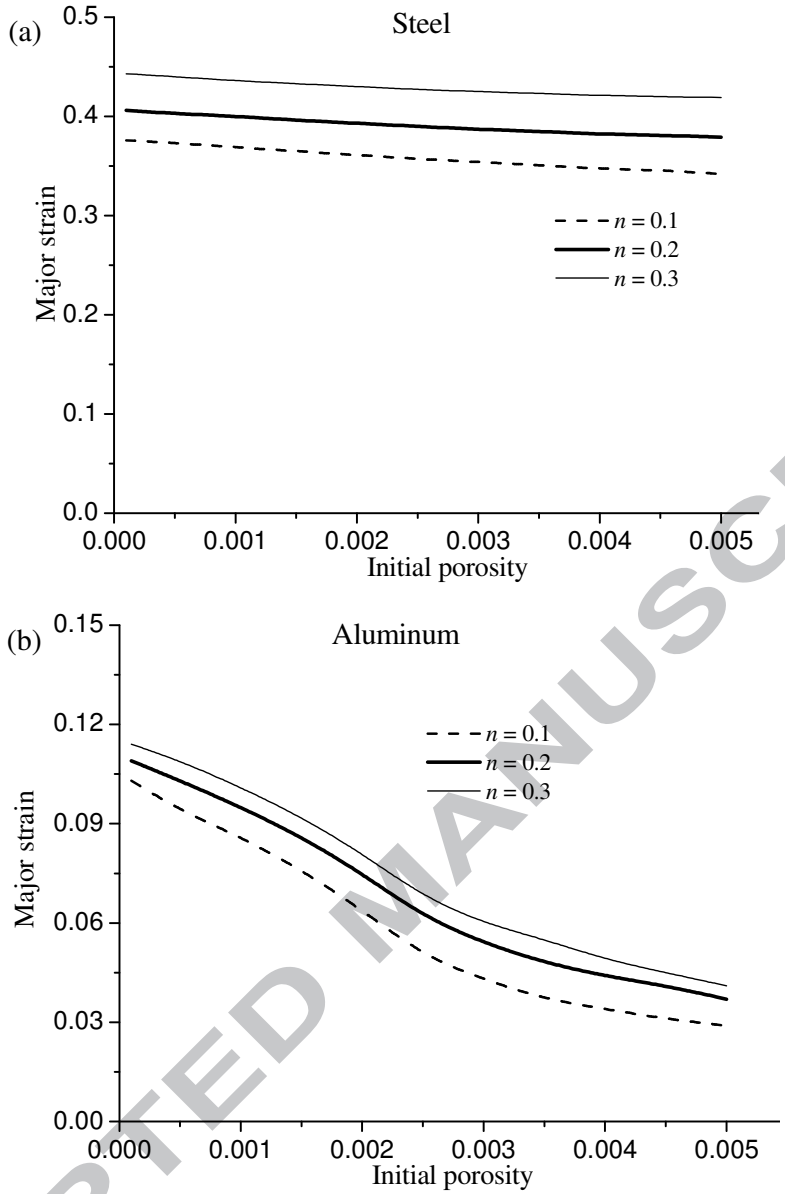

Fig. 7. Effect of the hardening exponent n on the critical localization strain (along the PST loading path) for different initial porosities: (a) steel and (b) aluminum alloy.

4.2 Case of q-parameter calibration

The results obtained in the previous section have shown that the hardening parameters of the fully dense matrix material have little effect on the ductility limit predictions in the case of the approach that considers the GTN model, with strain-controlled nucleation, coupled with the Rice bifurcation criterion. More specifically, the porosity evolution was found to be independent of strain hardening, leading to strain localization essentially controlled by the damage parameters. This limitation of the original Gurson model has been pointed out by Leblond et al. (1995), who proposed an improvement to the Gurson model in order to account for strain hardening effects on porosity evolution. On the other hand, following the earlier work of Tracey (1971), Faleskog et al. (1998) proposed a micromechanics-based calibration for the q-parameters (see Eq. (7)), in order to take into consideration the effects of strain hardening and material strength on void growth. Table 5 summarizes the calibrated q-parameters for different hardening exponents and yield strength (σ_0/E), as taken from Faleskog et al. (1998).

Table 5

Calibrated q_1 and q_2 parameters for the GTN model (from Faleskog et al. (1998)).

Hardening exponent n	$\sigma_0/E = 0.001$		$\sigma_0/E = 0.002$	
	q_1	q_2	q_1	q_2
0.025	1.880	0.956	1.840	0.977
0.05	1.630	0.950	1.570	0.974
0.10	1.580	0.902	1.460	0.931

The GTN model with strain-controlled nucleation is considered again in this section. The damage parameters used in the simulations are listed in Table 6. In Faleskog et al. (1998), the

calibration of the q-parameters has been achieved based on the following hardening power law:

$$\frac{\sigma_{\mathrm{M}}}{\sigma_0}=\left(\frac{\sigma_{\mathrm{M}}}{\sigma_0}+\frac{E}{\sigma_0}\bar{\varepsilon}_{\mathrm{M}}^{pl}\right)^n . \tag{28}$$

Table 6

Damage parameters for the GTN model with strain-controlled nucleation.

Material	f_0	s_N	ε_N	f_N	f_{cr}	δ_{GTN}
Steel	0.001	0.1	0.50	0.040	0.040	5

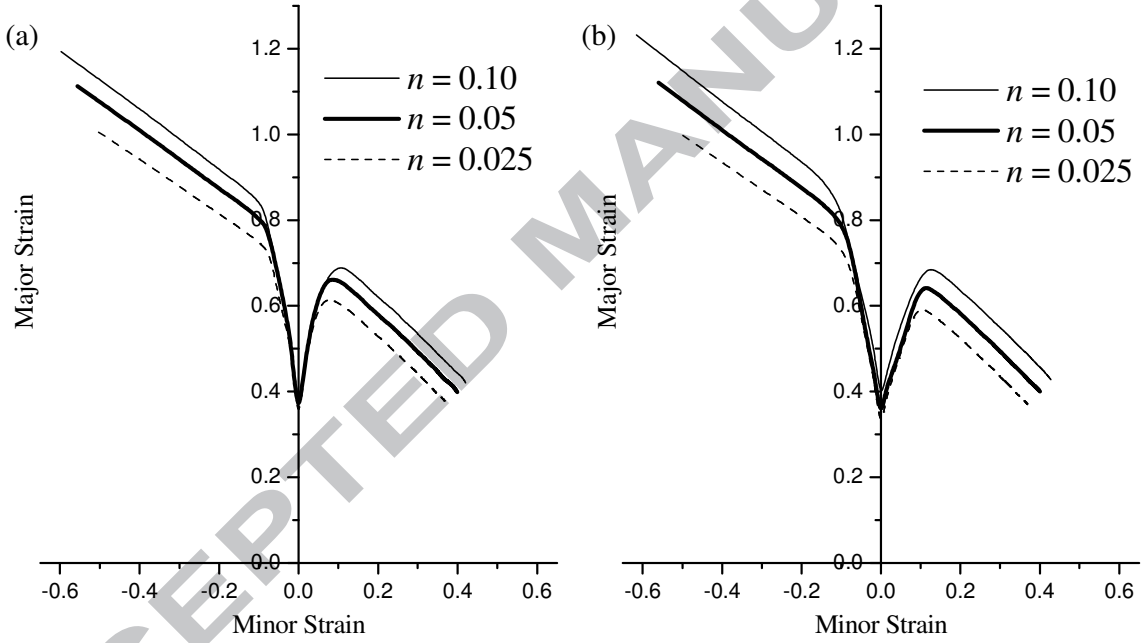

Fig. 8. Effect of the hardening exponent n on the prediction of the ELDs for the steel material with: (a) $\sigma_0/E=0.001$ and (b) $\sigma_0/E=0.002$.

Figure 8 shows the influence of the hardening exponent n of the power law (see Eq. (28)) on the predicted ELDs for the studied steel material. In contrast to the previous analysis with constant q-parameters (see section 4.1), the use of micromechanics-based calibrated q-parameters, as suggested by Faleskog et al. (1998), allows the effect of strain hardening on

strain localization predictions to be reproduced. As shown in Fig. 8, increasing the hardening exponent n leads to an increase in the ductility limits. This effect is more perceptible in the left and right-hand sides of the ELDs, namely for strain paths located in the neighborhood of the UT and BBT domains. This trend is consistent with the literature results, where it has been shown that strain hardening has a non-negligible effect on material ductility (see, e.g., Stören, and Rice, 1975; Doghri and Billardon, 1995; Hora et al., 1996; Zhao et al., 1996). Furthermore, the effect of strain hardening on the stress–strain response and on the evolution of void volume fraction for three representative loading paths, namely the UT, PST and BBT strain paths, is illustrated in Figs. (9)–(11) with $\sigma_0/E = 0.001$. These figures reveal clearly that, when the GTN q-parameters are adjusted according to the calibration scheme proposed by Faleskog et al. (1998), the hardening characteristics show a significant influence on the porosity evolution and therefore on strain localization predictions, in contrast to the case of constant q-parameters. Similar results have been obtained with $\sigma_0/E = 0.002$ and are not reported here for conciseness. As a consequence, the present results suggest that when the GTN model, with strain-controlled nucleation, is combined with bifurcation analysis to predict material ductility, the q-parameters should be physically calibrated (e.g., according to the works of Faleskog et al. (1998)), in order to account for the effect of strain hardening on void growth, and hence on material ductility.

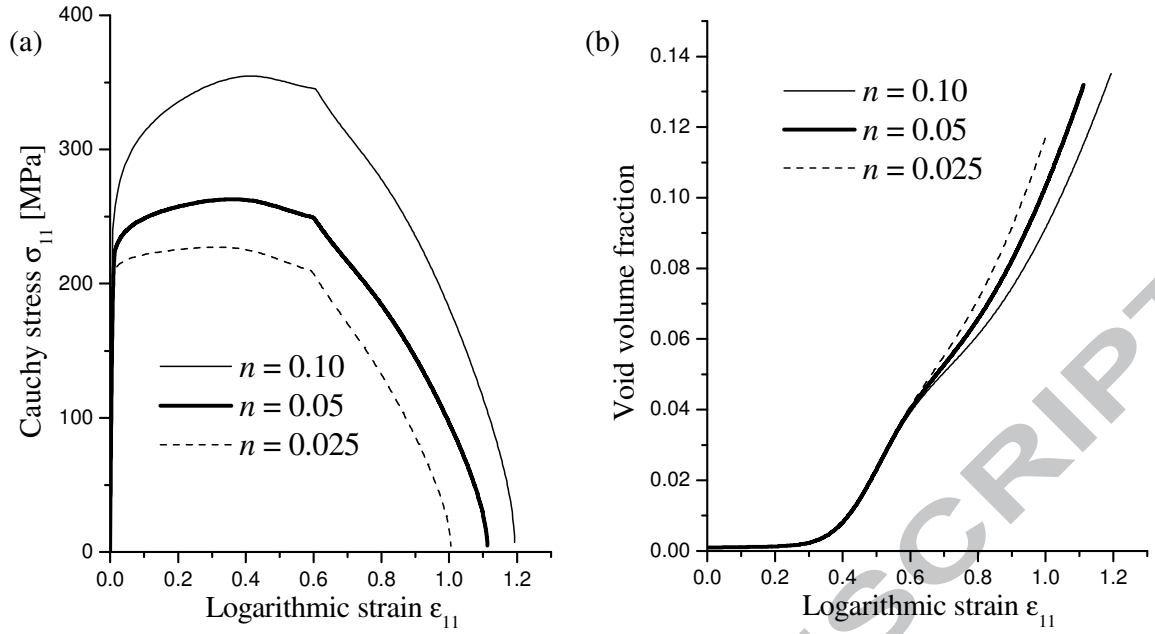

Fig. 9. Effect of the hardening exponent n on the evolution of the Cauchy stress and void volume fraction, along the UT loading path up to localization, for the steel material with $\sigma_0/E = 0.001$.

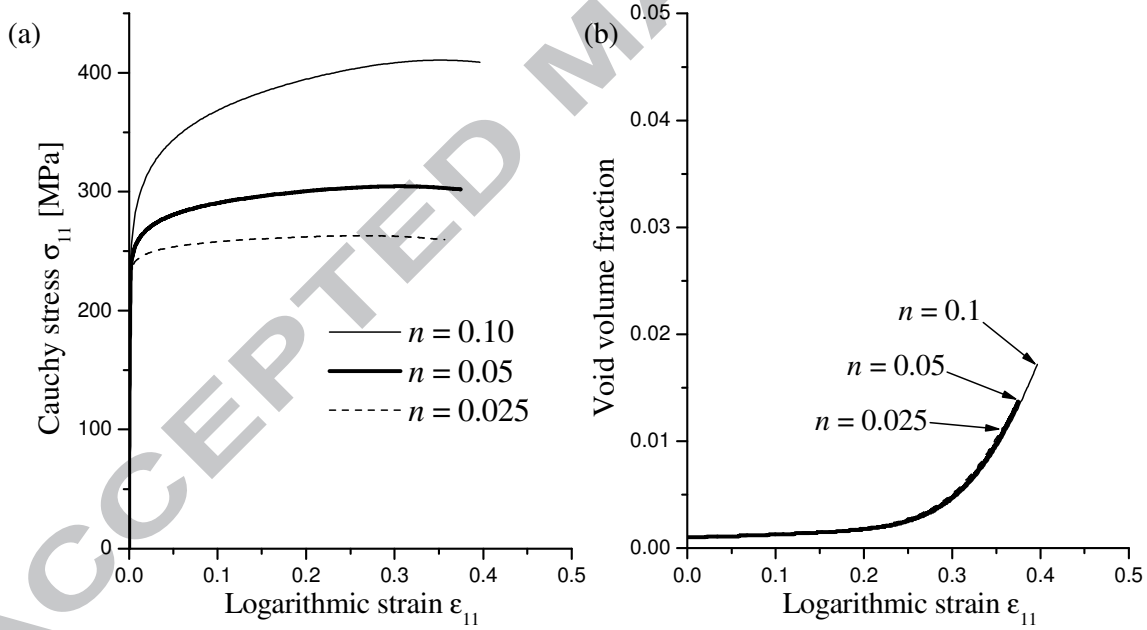

Fig. 10. Effect of the hardening exponent n on the evolution of the Cauchy stress and void volume fraction, along the PST loading path up to localization, for the steel material with $\sigma_0/E = 0.001$.

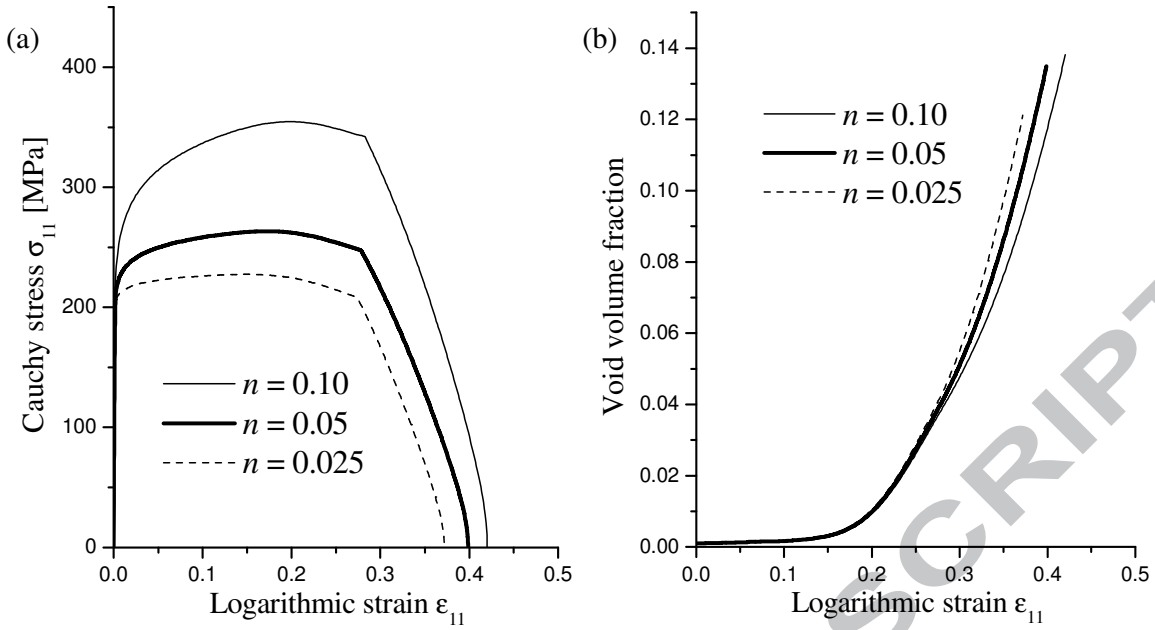

Fig. 11. Effect of the hardening exponent n on the evolution of the Cauchy stress and void volume fraction, along the BBT loading path up to localization, for the steel material with $\sigma_0/E = 0.001$.

4.3 Case of stress-controlled nucleation

In this section, the effect of strain hardening on strain localization is investigated using the GTN model with stress-controlled nucleation. More specifically, the non-normality in the plastic flow rule, resulting from this choice of nucleation criterion, is considered here. The motivation behind this constitutive framework that involves non-associated plasticity is an attempt to incorporate some strain hardening effects on void growth and, consequently, on strain localization.

The GTN parameters q_1 and q_2 used in the simulations do not depend on the matrix hardening characteristics and are taken equal to those used in section 4.1 (see Tvergaard, 1981). Also, the strain hardening of the fully dense matrix material is modeled with the Ludwig isotropic hardening law, as described in Eq. (20). A fictitious aluminum alloy is considered in this study, mainly for qualitative results and illustrative purposes. The

corresponding elastic–plastic and damage parameters, for the GTN model with stress-controlled nucleation, are summarized in Tables 7 and 8, respectively.

Table 7

Elastic properties and Ludwig hardening parameters for the studied material.

Material	E (MPa)	ν	σ_0 (MPa)	k (MPa)	n
Aluminum	70,000	0.33	150	500	0.1-0.2-0.3

Table 8

Damage parameters for the GTN model with stress-controlled nucleation.

Material	f_0	s_N	σ_N (MPa)	f_N	f_{cr}	δ_{GTN}	q_1	q_2	q_3
Aluminum	0.001	0.1	0.27	0.035	0.00213	10	1.5	1.0	2.15

The effect of the strain hardening exponent n on the predicted ELDs for the studied material is illustrated in Fig. 12. It can be observed that the consideration of non-normality, due to stress-controlled nucleation (see Eq. (12)), allows the non-negligible sensitivity of material ductility to strain hardening to be reproduced. Indeed, for the studied aluminum alloy (Fig. 12), the predicted ductility limits are found directly proportional to the hardening exponent n for all strain paths. This result is consistent with the well-known effect of strain hardening on material formability, which has been reported in a number of literature works that adopted different constitutive equations in conjunction with various plastic instability criteria (see, e.g., Stören and Rice, 1975; Needleman and Rice, 1978; Doghri and Billardon, 1995; Hora et al., 1996; Zhao et al., 1996).

In order to provide further explanation to the above results, Figs. 13–15 depict the evolution of the Cauchy stress and void volume fraction, up to localization, for the studied aluminum alloy along the particular strain paths of UT, PST and BBT. For these three strain paths, one can clearly observe that the porosity evolution is significantly affected by the strain hardening characteristics in the present case of stress-controlled nucleation (see Figs. 13–15),

in contrast to the case of strain-controlled nucleation (see Fig. 5(b)). This dependence of void growth on material hardening allows, in turn, the effect of strain hardening on strain localization to be accounted for. Moreover, this non-normality in the plastic flow rule plays a destabilizing role in the localization bifurcation analysis. This destabilizing effect can be observed for all of the strain paths, and especially for the PST strain path, where bifurcation is predicted for positive hardening moduli (see Fig. 14(a)). These results are in agreement with those reported in Needleman and Rice (1978), where the original Gurson model with stress-controlled nucleation was considered. For the UT and BBT strain paths, the Cauchy stress–strain curves reported in Figs. 13(a) and 15(a) reveal that the critical hardening moduli are not strongly negative, as compared to those obtained in the case of strain-controlled nucleation (see section 4.1). This feature helps in reproducing the important effect of strain hardening on material ductility.

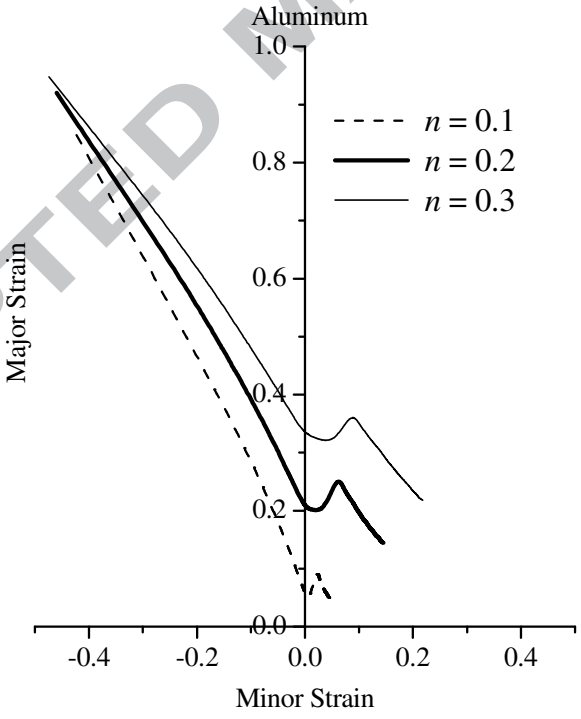

Fig. 12. Effect of the hardening exponent n on the prediction of ELDs for the studied aluminum alloy.

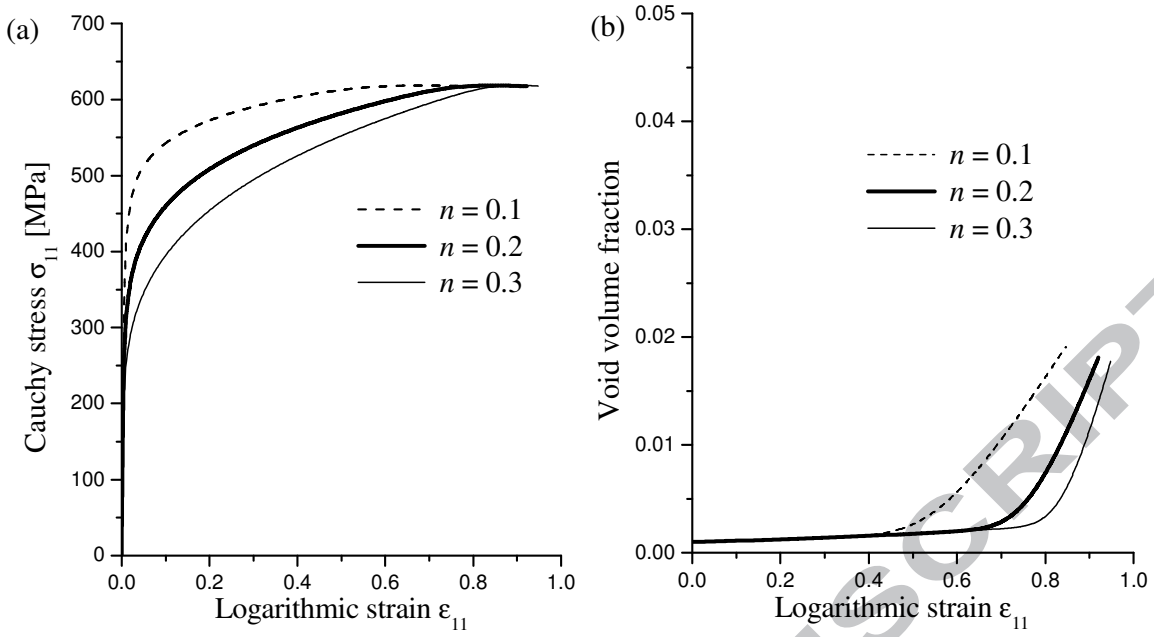

Fig. 13. Stress–strain responses and void volume fraction evolution, up to localization, along the UT strain path for the aluminum alloy.

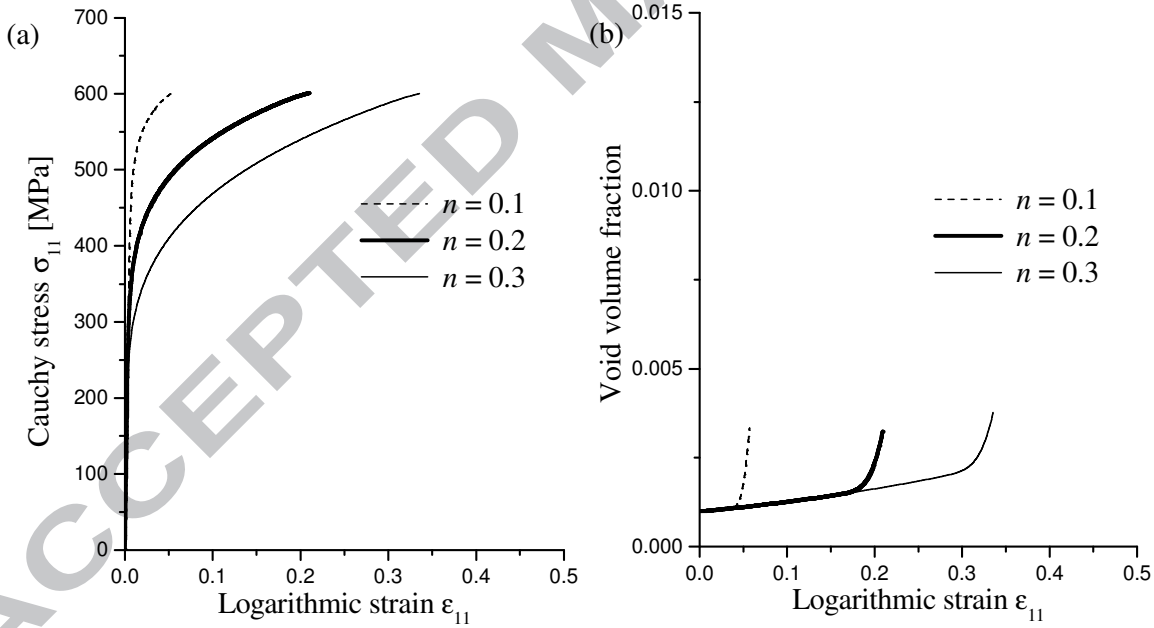

Fig. 14. Stress–strain responses and void volume fraction evolution, up to localization, along the PST strain path for the aluminum alloy.

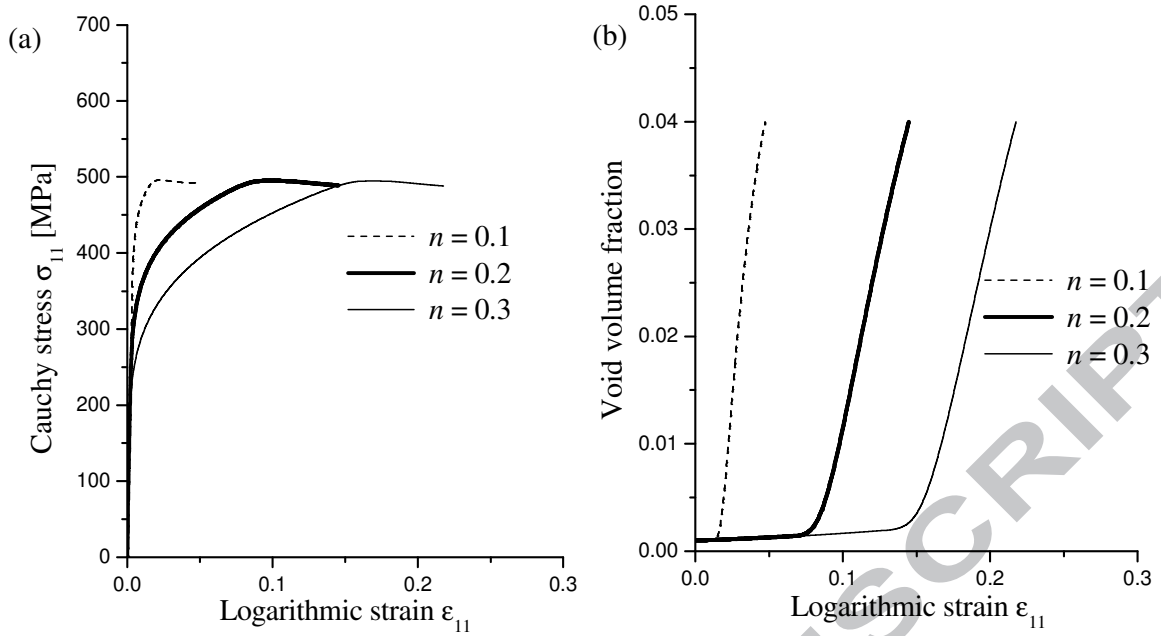

Fig. 15. Stress–strain responses and void volume fraction evolution, up to localization, along the BBT strain path for the aluminum alloy

5 Conclusions

In the present study, the sensitivity of the ductility limits of porous materials to the dense matrix strain hardening has been investigated. For this purpose, the so-called GTN ductile damage model with isotropic hardening has been implemented into the finite element software ABAQUS/standard in the framework of large plastic strains and a fully three-dimensional formulation. The resulting model has been coupled with the Rice bifurcation criterion to predict the ductility limits set by plastic strain localization. For completeness and comparison purposes, two different void nucleation mechanisms have been explored in the GTN model. First, strain-controlled nucleation has been considered, as initially suggested by Gurson (1977), which represents the most commonly adopted modeling for the nucleation of new voids in Gurson-type models. Then, stress-controlled nucleation is introduced, which relies on the maximum stress in the particle–matrix interface. It is worth noting that when nucleation is stress-controlled, the normality of the plastic flow rule does not hold, which brings a destabilizing effect that promotes the initiation of localization bifurcation. A third

alternative modeling for the analysis of hardening effects on strain localization has also been explored, which consists in adopting a micromechanics-based calibration for the GTN q-parameters (see, e.g., Faleskog et al., 1998). One of the main interests in this physically-based calibration is to allow the impact of strain hardening on void growth to be accounted for, which allows in turn reproducing the effect of hardening on strain localization predictions through the proposed coupling between the GTN model and the Rice bifurcation criterion.

In the case of strain-controlled nucleation, varying the hardening exponent in the Ludwig isotropic hardening law was found to produce negligibly small effects on the ductility limit predictions for both aluminum alloys and steel materials. More specifically, for most of the strain paths considered, the ductility limits predicted by the present approach were found almost insensitive to the material hardening, while a slightly more noticeable effect was observed for the particular plane strain loading path. These findings are mainly attributable to the porosity evolution in the Gurson model, which is strain hardening-independent in the case of strain-controlled nucleation.

In order to account for the effect of hardening on strain localization, the GTN q-parameters, associated with strain-controlled nucleation, were taken to follow the micromechanics-based calibration suggested by Faleskog et al. (1998). Two materials with different yield strengths were considered. For both materials, the corresponding new predictions revealed clear sensitivity of the porosity evolution to the hardening characteristics, in contrast to the previously studied case of constant q-parameters. In the same way, the effect of hardening on the ductility limit predictions, set by plastic flow localization, was clearly reproduced for all strain paths.

Finally, when stress-controlled nucleation is considered in the GTN model, the porosity evolution was shown to be significantly affected by the strain hardening characteristics, which

in turn is likely to influence the strain localization predictions. Indeed, the predicted ductility limits were found to be proportional to the hardening exponent of the fully dense matrix material for all of the strain paths considered. This important effect of strain hardening on material ductility was reproduced within this constitutive framework thanks to the destabilizing role of the non-normality in the plastic flow rule, which precipitates earlier initiation of strain localization.

References

Abed-Meraim, F., Balan, T., Altmeyer, G., 2014. Investigation and comparative analysis of plastic instability criteria: application to forming limit diagrams. International Journal of Advanced Manufacturing Technology 71, 1247–1262.

Aravas, N., 1987. On the numerical integration of a class of pressure-dependent plasticity models. International Journal for Numerical Methods in Engineering 24, 1395–1416.

Benzerga, A.A., Besson, J., 2001. Plastic potentials for anisotropic porous solids. European Journal of Mechanics – A/Solids 20, 397–434.

Brunet, M., Mguil, S., Morestin, F., 1998. Analytical and experimental studies of necking in sheet metal forming processes. Journal of Materials Processing Technology 80-81, 40–46.

Chu, C., Needleman, A., 1980. Void nucleation effects in biaxially stretched sheets. Journal of Engineering Materials and Technology 102, 249–256.

Considère, A., 1885. Mémoire sur l'emploi du fer et de l'acier dans les constructions. Ann. Ponts et Chaussées 9, 574–775.

Doghri, I., Billardon, R., 1995. Investigation of localization due to damage in elasto-plastic materials. Mechanics of Materials 19, 129–149.

Faleskog, J., Gao, X., Shih, C.F., 1998. Cell model for nonlinear fracture analysis – I. Micromechanics calibration. International Journal of Fracture 89, 355–373.

Gao, X., Faleskog, J., Shih, C .F., 1998. Cell model for nonlinear fracture analysis – II. fracture-process calibration and verification. International Journal of Fracture 89, 375–398.

Goodwin, G., 1968. Application of strain analysis to sheet metal forming problems in the press shop. SAE Technical Paper No. 680093.

Gurson, A.L., 1977. Continuum theory of ductile rupture by void nucleation and growth: Part I – yield criteria and flow rules for porous ductile media. ASME Journal of Engineering Materials and Technology 99, 2–15.

Haddag, B., Abed-Meraim, F., Balan, T., 2009. Strain localization analysis using a large deformation anisotropic elastic–plastic model coupled with damage. International Journal of Plasticity 25, 1970–1996.

Hill, R., 1952. On discontinuous plastic states, with special reference to localized necking in thin sheets. Journal of the Mechanics and Physics of Solids 1, 19–30.

Hill, R., 1958. A general theory of uniqueness and stability in elastic–plastic solids. Journal of the Mechanics and Physics of Solids 6, 236–249.

Hora, P., Tong, L., Reissner, J., 1996. A prediction method of ductile sheet metal faillure in FE simulation. Numisheet, 252–256. Michigan USA.

Kachanov, L. M., 1986. Introduction to continuum damage mechanics. Netherlands: Springer.

Keeler, S., Backofen, W.A., 1963. Plastic instability and fracture in sheets stretched over rigid punches. ASM Transactions Quarterly 56, 25–48.

Kojic, M., 2002. Stress integration procedures for inelastic material models within finite element method. ASME Applied Mechanics Reviews 55, 389–414.

Leblond, J.B., Perrin, G., Devaux, J., 1995. An improved Gurson-type model for hardenable ductile metals. European Journal of Mechanics – A/Solids 14, 499–527.

Lemaitre, J. 1985. A continuous damage mechanics model for ductile fracture. ASME Journal of Engineering Materials and Technology 107, 83–89.

Lemaitre, J., 1992. A course on damage mechanics. Berlin: Springer.

Li, Y.-F., Nemat-Nasser, S., 1993. An explicit integration scheme for finite-deformation plasticity in finite-element methods. Finite Elements in Analysis and Design 15, 93–102.

Mansouri, L.Z., Chalal, H., Abed-Meraim, F., 2014. Ductility limit prediction using a GTN damage model coupled with localization bifurcation analysis. Mechanics of Materials 76, 64–92.

Marciniak, Z., Kuczynski, K., 1967. Limit strains in the process of stretch forming sheet metal. International Journal of Mechanical Sciences 9, 609–620.

Needleman, A., Rice, J.R., 1978. Limits to ductility set by plastic flow localization. In: D.P. Koistinen, N.M. Wang (Eds.), Mechanics of sheet metal forming. New York: Plenum Press, 237–267.

Oliver, J., Huespe, A., Blanco, S., Linero, D., 2005. Stability and robustness issues in numerical modeling of material failure with the strong discontinuity approach. Computer Methods in Applied Mechanics and Engineering 195, 7093–7114.

Rice, J.R., 1976. The localization of plastic deformation. Theorical and Applied Mechanics. Koiter ed., 207–227.

Rudnicki, J.W., Rice, J.R., 1975. Conditions for the localization of deformation in pressure sensitive dilatant materials. Journal of the Mechanics and Physics of Solids 23, 371–394.

Saje, M., Pan, J., Needleman, A., 1982. Void nucleation effects on shear localization in porous plastic solids. International Journal of Fracture 19, 163–182.

Stören, S., Rice, J.R., 1975. Localized necking in thin sheets. Journal of the Mechanics and Physics of Solids 23, 421–441.

Swift, H.W., 1952. Plastic instability under plane stress. Journal of the Mechanics and Physics of Solids 1, 1–18.

Tracey, D.M., 1971. Strain-hardening and interation effects on the growth of voids in ductile fracture. Engineering Fracture Mechanics 3, 301–315.

Tvergaard, V., 1981. Influence of voids on shear band instabilities under plane strain conditions. International Journal of Fracture 17, 389–407.

Tvergaard, V., 1982a. Ductile fracture by cavity nucleation between larger voids. Journal of the Mechanics and Physics of Solids 30, 265–286.

Tvergaard, V., 1982b. Influence of void nucleation on ductile shear fracture at a free surface. Journal of the Mechanics and Physics of Solids 30, 399–425.

Tvergaard, V., 1982c. Material failure by void coalescence in localized shear bands. International Journal of Solids and Structures 18, 659–672.

Tvergaard, V., Needleman, A., 1984. Analysis of the cup-cone fracture in a round tensile bar. Acta Metallurgica 32, 157–169.

Valanis, K.C., 1989. Banding and stability in plastic materials. Acta Mechanica 79, 113–141.

Yamamoto, H., 1978. Conditions for shear localization in the ductile fracture of void-containing materials. International Journal of Fracture 14, 347–365.

Zhao, L., Sowerby, R., Sklad, M.P., 1996. A theoretical and experimental investigation of limit strains in sheet metal forming. International Journal of Mechanical Sciences 38, 1307–1317.

Research highlights

- The GTN model is combined with bifurcation theory to predict ductility limits of porous materials.
- The sensitivity of ductility limit predictions to the strain hardening characteristics is investigated.
- Strain hardening effects on strain localization depend on the selected void nucleation mechanism.
- Non-normality induced by stress-controlled nucleation allows reproducing strain hardening effects.
- Micromechanics-based q-parameter calibration allows strain hardening effects to be accounted for.